CEAS Aeronautical Journal (2023) 14:281–293
https://doi.org/10.1007/s13272-022-00635-w

ORIGINAL PAPER

Recent developments of common numerical methods and common experimental means within the framework of the large passenger aircraft program

F. Boden[1] · H. P. Barth[1] · S. Hein[1] · D. Heitmann[4] · T. Kirmse[1] · C. Klein[1] · W. Krüger[2] · J. Lemarechal[1] · M. Norambuena[2] · D. Schäfer[2] · R. Schnell[3] · K. Sinha[2] · A. Theiß[1] · A. Weiss[1]

Received: 15 December 2021 / Revised: 24 November 2022 / Accepted: 20 December 2022 / Published online: 16 January 2023

Abstract

For the exploration and validation of the integration of efficient propulsion concepts and new technologies for future large passenger aircraft, it is necessary to establish suitable design, evaluation and measurement tools. Therefore, as one major activity of the Large Passenger Aircraft (LPA) Platform 1 of the Clean Sky 2 initiative, the so-called Cross-Capability Demonstrator (XDC), has been set up to develop and demonstrate powerful numerical and experimental methods for aerodynamic, aeroacoustics, and aeroelastic simulation and measurement tasks. The paper will give an overview of the activities to be performed within the XDC and present some of the latest achievements related to this demonstrator.

Keywords Experimental means · Numerical means · Prediction methods · XDC · Jet flap interaction · Vibration testing · Optical methods

Abbreviations

1MG	1-Meter wind tunnel Göttingen
3D	3-Dimensional
A/C	Aircraft
BLI	Boundary layer ingestion
CAA	Computational aeroacoustics
CFD	Computational fluid dynamics
CFI	Cross-flow instabilities
CNT	Carbon nanotubes
CS2	Clean sky 2
DLM	Boublet lattice method
DLR	German aerospace center
ESS	Engine section stator
FM-BEM	Fast multipole boundary element method
FRPM	Fast random particle mesh
FW-H	Ffowcs Williams and Hawkings
F_{xyz}	Force in x-, y-, z-direction
HTTP	Horizontal tail plane
IBC	Immersed boundary conditions
IPCT	Image pattern correlation technique
iPSP	Instationary pressure-sensitive paint
LED	Light-emitting diode
LES	Large Eddy simulation
LPA	Large passenger aircraft
Ma	Mach number
MIMO	Multiple input multiple output
M_{xyz}	Moment around x-, y-, z-axis
NLDE	Non-linear disturbance equations
NLR	Netherlands aerospace center
NOLOT	Non-local transition analysis
OGV	Outlet guide vane
OR	Open rotor engine
PIANO	CAA code developed by DLR
PSP	Pressure-sensitive paint
RANS	Reynolds averaged Navier–Stokes
Re	Reynolds number
RTG	Rotor test rig Göttingen
SA^2FIR	Simulator of aerodynamic and acoustic fan integration
SFB	German "Sonderforschungsbereich"

✉ F. Boden
fritz.boden@dlr.de

[1] Institute of Aerodynamics and Flow Technology, Bunsenstr. 10, 37073 Göttingen, Germany

[2] Institute of Aeroelasticity, Bunsenstr. 10, 37073 Göttingen, Germany

[3] Institute of Propulsion Technology, Linder Höhe, 51147 Cologne, Germany

[4] Institute of Aerodynamics and Flow Technology, Lilienthalplatz 7, 38108 Brunswick, Germany

SISO	Single-input single-output
SPECTRA	SwePt flat plate crossflow transition
T–S	Tollmien–Schlichting
TSP	Temperature-sensitive paint
UHBR	Ultra-high bypass ratio engine
URANS	Unsteady Reynolds averaged Navier–Stokes
VLM	Vortex lattice method
w/o	Without
XDC	Cross-capability demonstrator

1 Introduction

The main objective of the Clean Sky 2 (CS2) Large Passenger Aircraft (LPA) Platform 1 is the exploration and validation of the most efficient future propulsion systems for the next generation short-, medium-, and long-range aircraft. Among others, advanced propulsion systems like Ultra-High Bypass Ratio (UHBR) engines, Open Rotor (OR) propulsion, or Boundary Layer Ingestion (BLI) systems are assessed with respect to their related benefit like reduced fuel burn and noise emissions. To quantify the impact of the integration of these advanced propulsion systems to the airframe, it is important to have suitable tools for prediction, optimization and evaluation available.

Thus, within LPA Platform 1, the so-called Cross-Capability Demonstrator (XDC) has been set up for the development, demonstration, and maturation of advanced numerical methods and experimental means. The XDC therefore includes two main streams — Common Numerical Methods and Common Experimental Means. In what follows, some examples from these two development streams are given.

1.1 Common numerical methods

Within the Common Numerical Methods stream mainly, numerical methods for the prediction of the aerodynamic, aeroacoustic, and aeroelastic behavior of the future propulsion concepts, as well as for the assessment of their interaction with the airframe are being developed.

Several design processes, assessment, and measurement tools are being established. The developed tools are meant to be applicable to all types of propulsion systems (e.g., UHBR, OR, BLI) and are required to quantify the impacts of theses advanced concepts by improved physical insight.

Below some example developments are briefly presented, such as the noise prediction for an installed UHBR engine, the simulation of jet-flap interference noise, and the investigation of rotational effects on boundary layer instabilities.

Additionally, examples regarding the design of a fan using numerical design tools and the prediction of the aeroelastic behavior of aircraft with integrated propulsion, including a T-tail flutter analysis, are described.

1.1.1 Aeroacoustic investigations on UHBR noise emission

Within the XDC demonstrator, different methods for the assessment of UHBR engine noise were developed and implemented into the CAA code PIANO. This includes fan tone shielding predictions at the A/C airframe by means of unsteady fan modes imposed on specified planes in the intake of the engine. Furthermore, fan installation effects from inhomogeneous flows with a newly developed ducted rotor model are informed by actuator disk RANS.

As another topic, scale-resolving methods for the assessment of jet-flap interference noise have been studied, specifically addressing the effect of jet temperature on installation noise.

The computations have been conducted with the DLR-PIANO code [1]. PIANO applies fourth-order dispersion optimized numerical schemes in combination with block structured curvilinear and hierarchical Cartesian meshes with hanging nodes at inner boundaries. Linear or non-linear governing equations are applied in perturbation form over a steady background flow that is provided by preceding RANS simulation.

1.1.2 Numerical predictions on installed UHBR

In the past, UHBR installation noise computations were based on URANS simulations with subsequent Ffowcs Williams and Hawkings (FW-H) extrapolation, see e.g., [2].

However, to account for the effect of the airframe in the FW-H extrapolation step, this would require the inclusion of the entire airframe surface into the FW-H surface integral. If unsteady data are not known a priori, the explicit FW-H surface integral changes into an integral equation problem that can be very efficiently solved by means of a Fast Multipole Boundary Element Method (FM-BEM). Within the XDC, such an approach was studied to predict fan mode shielding at the A/C airframe. Furthermore, in the present task, an acoustic model for the installation noise effect of the disturbed fan was developed and implemented into the CAA code PIANO to account for non-uniform flow effects on installation noise and sound propagation. The model is an extension of a propeller model presented in [3] and based on rotating point or line sources instead of resolving the rotor geometry. The newly developed tool was tested with the UHBR engines of the SFB 880 A/C. An immersed boundary condition (see [4]) was adopted and extended for the meshing of this geometry on a hierarchical Cartesian mesh with several refinement levels. Figure 1 depicts the CAA computational domain and the A/C geometry. The grid consists of 1,944 cubic blocks, all of them containing the same number of points. The blocks close to the geometry are smaller, indicating the refinement toward the surfaces. In total, the grid comprises 414.6 million points. In Fig. 2, the

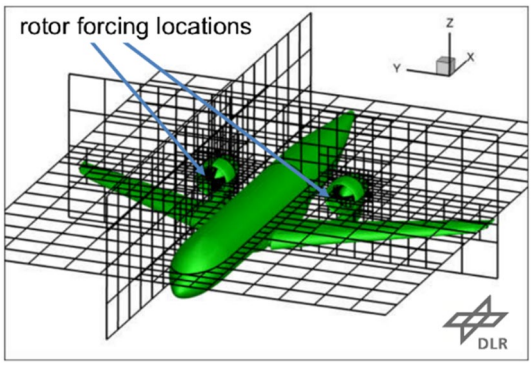

Fig. 1 CAA computational domain utilizing immersed boundary conditions (IBC) to resolve the entire A/C geometry with a Cartesian block structured mesh and refinement zones based on hanging nodes; 400 M mesh points for 2 kHz resolution

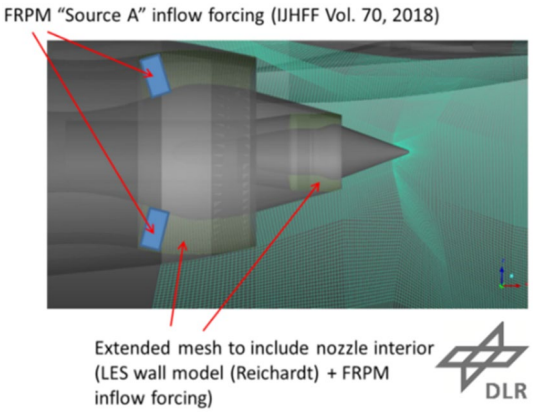

Fig. 3 Cross-sectional view through UHBR and indicated inflow-forcing locations

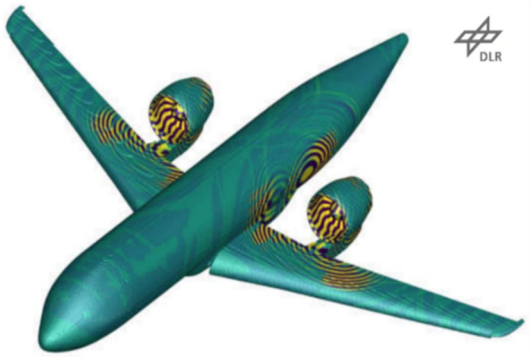

Fig. 2 Acoustic pressure signature of UHBR on wing and fuselage using immersed boundary conditions to resolved the entire aircraft geometry

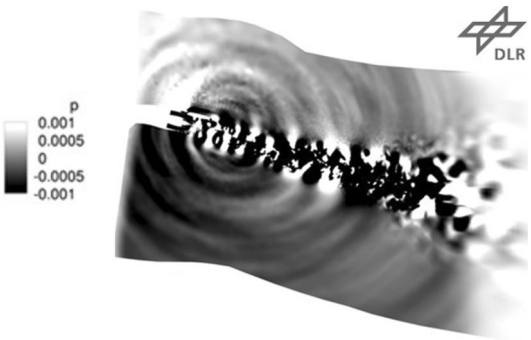

Fig. 4 Snapshot of acoustic pressure fluctuations as consequence of jet-flap interaction

A/C surface is shown color-coded with the acoustic pressure fluctuations at a random time instance. The acoustic waves emanating from the UHBR and their footprint on wing and fuselage are clearly visible. With the newly developed noise source model and utilizing an immersed boundary description on a hierarchical Cartesian mesh, the PIANO code becomes capable of computing UHBR sound emission and installation effects in non-uniform flow very efficiently for complex geometries.

1.1.3 Numerical predictions on jet-flap interference noise and the effect of the jet temperature

For scale-resolving simulations, the PIANO code is used with nonlinear disturbance equations (NLDE) on curvilinear structured multi-block meshes. The approach can be deemed to represent a zonal LES approach where the resolved disturbances represent the unsteady fluctuations and steady mean-flow correction to the steady RANS background field. Recent work has shown that the NLDE formulation furthermore provides an implicit turbulent wall model that lowers wall resolution requirements. For efficient scale-resolving simulations on coarse grids, an active backscatter model was implemented into the PIANO code, see [5]. In this model, fluctuations are injected that contribute to the development of noise-generating vorticity fluctuations and furthermore, account for the effect of the non-resolved scales onto the resolved ones. With this approach, jet-flap interference noise has already been computed in the past, see e.g., [6]. In the current work, NLDE-LES simulations without turbulent backscatter have been applied to further study the effect of jet temperature on installed jet noise. In this application, it became necessary to trigger upstream turbulence with explicit stochastic volume forcing using the Fast Random Particle-Mesh (FRPM) method and Eddy relaxation source term. The fluctuations were generated inside the nozzle. The triggered turbulence essentially supports the development

of coherent flow structures in the jet shear layer that is important to capture the essential jet installation effect on sound. Figure 3 shows a slice through the UHBR and the location of the inflow forcing. The simulated noise field with expected features is shown in Fig. 4.

1.2 Transition analyses on a rotor blade

Spatial linear stability analyses are performed to study the laminar-turbulent transition in the boundary layer on the Z49 rotor, rotating in a $Ma_\infty = 0.75$ freestream. In a rotating reference frame, terms corresponding to Coriolis and centrifugal forces appear in the linearized disturbance equations. However, the effect of these rotational terms on the stability of boundary layers is only partially understood. Moreover, the terms are commonly neglected in an N-factor-based transition prediction framework. The main objective of the current work is to contribute to a better understanding of rotational effects on the stability of boundary layers located on industrially relevant geometries and to assess the extent to which the additional acceleration terms in a rotating reference frame need to be considered in an instability-based transition prediction framework. In addition, it is investigated whether rotation adds new kinds of instabilities, or rather alters transition mechanisms already existing in non-rotating cases. The model of interest belongs to a scaled version of the Z49 open rotor configuration with a front rotor radius of $R = 0.4295$ m rotating at 4503.27 rounds per minute. The freestream and open rotor operating conditions correspond to a typical nominal cruise condition and are as follows: $T_\infty = 283.95$ K and $p_\infty = 61,537$ Pa. The laminar basic flow, on which the linear instability analyses are performed, corresponds to the laminar region of a RANS computation, whose three-dimensional flow solution was kindly made available by Airbus.

To study the effect of rotation on the primary instability modes (i.e., Tollmien–Schlichting (T–S) and cross-flow instabilities (CFI)), the DLR in-house Parabolized Stability Equations-based code NOLOT is used, which has previously been extended to rotating reference frames [7]. The rotational terms' impact on the transition mechanisms is studied by neglecting or considering rotation in the linear local stability equations. An overview of the maximum local amplification rate (without rotational effects) of the Tollmien–Schlichting instability (TSI) in the laminar region on the rotor suction side is shown in Fig. 5. The area with the highest amplification rates on the suction side is located in the hub region. Thus, the highest N-factors are also to be expected there. The dashed lines in Fig. 5 indicate selected cuts for the N-factor integration, whereas the white lines correspond to the boundary-layer edge streamlines in the vicinity of the considered integration paths. In the following, the impact of the rotational terms on the stream-wise evolution of the N-factor envelope curves is discussed separately for the two primary instabilities considered (TSI and CFI). Figure 6(a) shows the N-factor envelope curves for four different line-in-flight cuts for the T–S wave computed with local stability theory (LST).

The N-factor for the integration path located the closest to the hub region ($r/R \approx 0.455$) reaches the highest value. As the distance from the axis of rotation increases, the maximum N-factor decreases. Thus, provided that the T–S wave

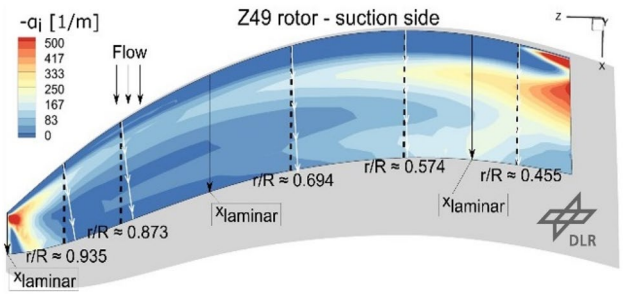

Fig. 5 Spatial growth rate distribution on the Z49's rotor suction side

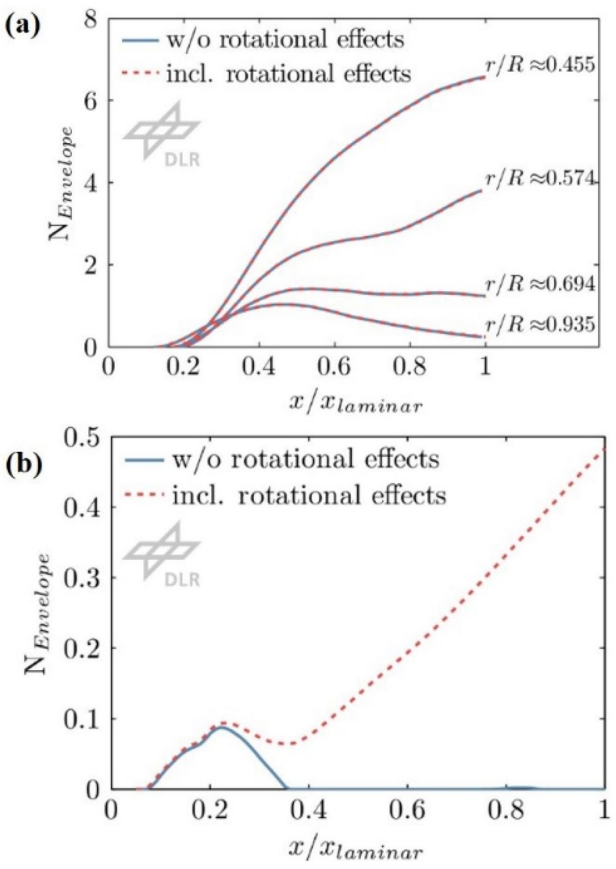

Fig. 6 Impact of the rotational effects on the stream-wise evolution of the N-factor envelope curve for **a** TSI and **b** CFI at r/R≈0.873

amplitudes are high enough, the laminar-turbulent transition is likely to first occur in the hub region. However, including the rotational effects in the LST has no impact on the transition scenario, since all curves shown in Fig. 6(a) coincide with the lines without rotational effects. On the other hand, Fig. 6(b) depicts the N-factor envelope curve for the cross-flow instability in the cut at $r/R \approx 0.873$. When neglecting the rotational effects, the region of amplified CFI extends to $x/x_{laminar} = 0.22$. On the other hand, including the rotational effects in the instability analysis, the CFI is amplified throughout the considered section. Thus, the maximum N-factor significantly exceeds the value without rotational effects. However, the gain in CFI amplitude is still too low to trigger transition (e.g., a transition N-factor of 7.6 is given in [8]). A possible reason for the different effects of rotation on T–S waves and cross-flow instabilities is seen in the wave propagation direction. In the study of Dechamps & Hein [7], it is shown that instabilities propagating normal to the flow direction are mostly affected by rotation, and that influence increases with rotation speed. The CFI propagates almost transverse to the main flow direction, whereas TSI is amplified at considerably lower wave angles. In this work, no new additional rotational instabilities were discovered, and it can be concluded that the inclusion of the rotational terms in the instability analysis hardly affects the instability characteristics of the Tollmien–Schlichting waves. On the other hand, cross-flow instabilities are destabilized by the effect of the rotational terms. Therefore, rotational effects should be considered in an N-factor-based transition framework.

1.3 Fan design for SA²FIR integration rig

In the given perimeter of Clean Sky, the DLR Institute of Propulsion Technology carried out the coupled aerodynamic and basic structural design of the fan stage for the SA²FIR integration rig [9]. The rig aims at experimentally investigating integration effects of future UHBR aero-engines in different high- and low-speed wind tunnels.

Basis of this design effort was a given full-scale and engine-realistic fan comprising the rotor, an outlet guide vane (OGV), and an engine sector stator (ESS). The design, also carried out at the Fan and Compressor Department of DLR, is summarized in [10] and was part of a propulsion system with the intake designed by Airbus in the context of the European initiative ASPIRE. The ongoing design efforts deal with the downscaling of the full scale to 26″ model scale and respective design adaptions necessary to deal with the change in Reynolds number and its impact on the given reference design. The current version of the resulting design is shown in Fig. 7. The downscaled version of the fan featured a composite blade material, and one important aspect of the concurrent aero- and structural design optimization

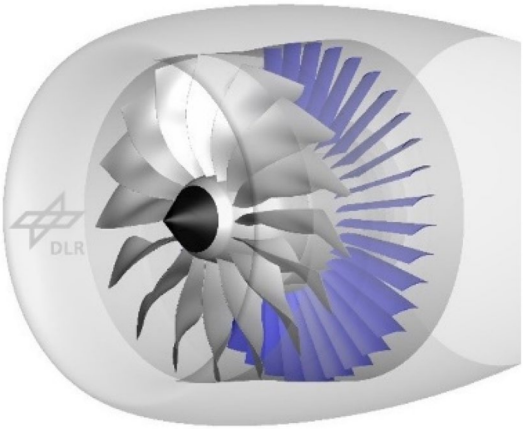

Fig. 7 Preliminary version of the SA²FIR rig featuring a 26″ fan as currently being designed by DLR in the CS2 perimeter

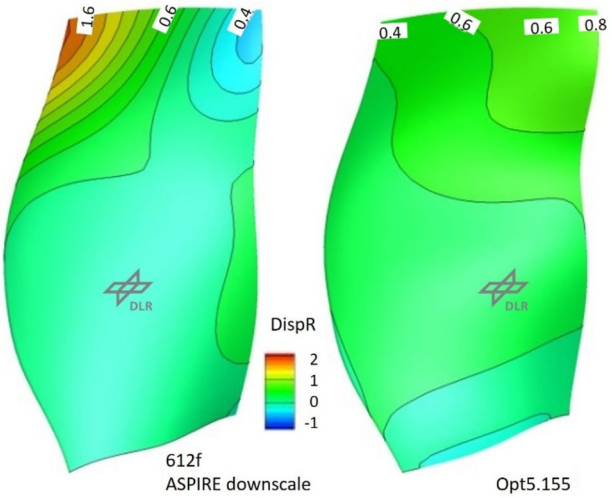

Fig. 8 Updated fan rotor design with composite material and minimized structural displacements in radial direction

was to minimize blade deformations due to centrifugal and pressure loads. The main results of this optimization effort are shown in Fig. 8 with the baseline displacements from original ASPIRE variant and the optimized displacement after the design adaptions yielding a reduction by a factor of 3 to 4.

This is a substantial achievement to ensure minimal tip gap for optimal aero and acoustic performance. The final blade will be manufactured by NLR as part of the SA²FIR rig. Apart from the rotor design, an updated OGV design was delivered with optimized 3D geometry features (see Fig. 9) as well as an ESS (see Fig. 10) to ensure an engine-realistic core flow. The design has passed a preliminary design review in Q1/2021 and will be finalized to carry out rig tests in Q2/2023.

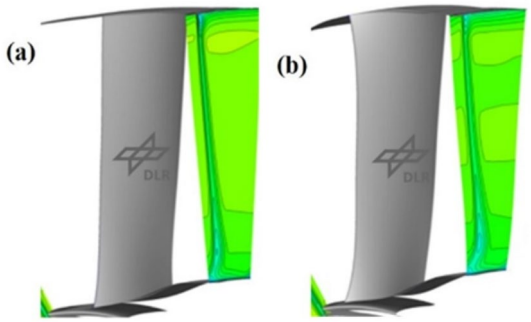

Fig. 9 **a** Optimized outlet guide vane (OGV) **b** with 3D design features (extracted planes show velocity contours downstream of the OGV)

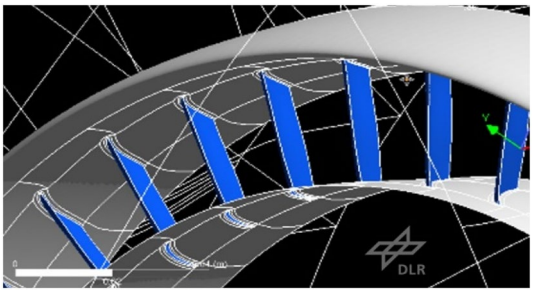

Fig. 10 Core section design including ESS

1.4 Aeroelastic simulation

1.4.1 Aeroelastic model of a reference configuration

For the development of numerical methods for aeroelastic analysis, vibration analyses as well as for vibro-acoustic analysis on future aircraft configurations, representative reference models for the aerodynamics, and the aircraft structure are necessary [11]. Only very few models with a sufficient level of detail are publicly available. In XCD, it was decided to base the aeroelastic reference model on the available, so-called DLR-D150 configuration [12] shown in Fig. 11. This model of an A320-size aircraft has been used for flight loads analysis in several DLR and German national (Lufo-) projects. Detailed wing models are available from those projects. The focus of the work in LPA has been the generation of fuselage and pylon models of sufficient details for aeroelastic and vibro-acoustic analysis. The modeling process used by DLR in LPA is MONA [13], consisting of the in-house development ModGen [14] and the commercial finite element software MSC Nastran. Basis of that process is the parametric modeling of wing and fuselage structures, allowing fast variations of design parameters, thus providing a basis for optimization. In MONA, three main steps are conducted—the parametric model setup, followed by an

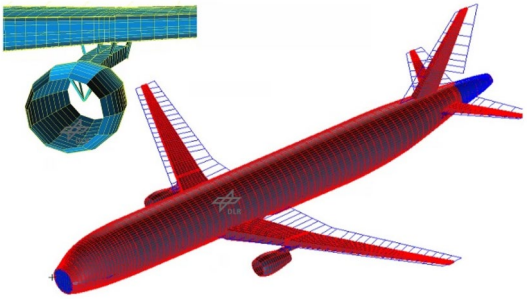

Fig. 11 Reference aircraft model (bottom) and detailed pylon interface modeling (top)

extensive load analysis campaign, and a structural optimization of the wing structures (this includes the main wings and the tailplane). Aeroelastic requirements like sufficient control surface efficiency are considered.

Finally, a full aircraft model is assembled. The full aircraft model comes with a grid for potential flow, i.e., Vortex- or Doublet-Lattice (VLM/ DLM) aerodynamics. More details can be found in [15]. For vibro-acoustic analysis, the modal characteristics of the structure are strongly impacted by the fidelity of the model. The degree of detail in the model influences how realistic the load transfer mechanisms within a structure are. In LPA, a structural model for investigations pertaining to engine vibration has been developed and exchanged with the project partners for numerical investigations. A modified pylon design was constructed for the D150 model, to replace the initially used beam models, for introducing engine vibrations into the wing structure, see Fig. 11, top. The modifications were done to achieve a realistic load transfer path and modal characteristics of the engine–pylon structure. The model of the engine load transmissibility to the rest of the aircraft structure has been verified by a transient analysis using SOL109 in MSC Nastran [16].

1.4.2 T-tail stability analysis

The conventional approach for flutter predictions heavily relies on the Doublet-Lattice Method (DLM) for computing subsonic unsteady aerodynamic forces. For this, aerodynamic forces induced by longitudinal and lateral displacements as well as rotations around the longitudinal and vertical axes are not considered. The steady-state aerodynamic forces are assumed to have no effect on the flutter onset either and ignored as well. Rear-mounted engines often require T-tail configurations. In the aeroelastic community, it is well known that those designs (like shown in Fig. 12, inset top right) feature adverse flutter characteristics which strongly depend on aerodynamic forces induced by in-plane and roll deformations of the horizontal tail plane (HTP)

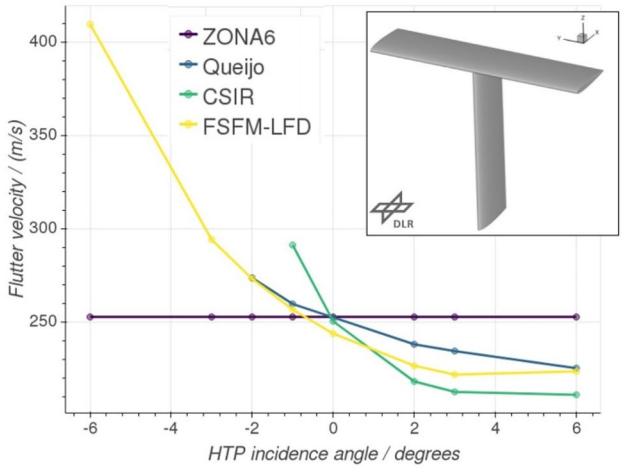

Fig. 12 Generic T-tail configuration (top) and resulting flutter speeds (bottom)

along with the steady aerodynamic trim forces [17]. It is therefore necessary to account for these additional aerodynamic forces in the flutter prediction of T- and H-tail configurations. Measures for this include corrections of DLM results by external methods, extensions of the DLM for the lacking degrees of freedom, unsteady Vortex Lattice Methods, and Computational Fluid Dynamics (CFD). The configuration for this study is a generic T-tail with un-swept and non-tapered vertical and horizontal tail planes based on [18]. The impact of the additional aerodynamic forces on the flutter points is studied by changing the steady horizontal tail plane (HTP) incidence angle and, hence, the steady aerodynamic loading on the HTP. For a subsonic Mach number of 0.4 and atmospheric at Mean Sea Level, the resulting flutter points are depicted in Fig. 12, bottom. The flutter onset predicted with the commonly used method (ZONA6) does neither depend on the steady HTP loading nor on lifting surface roll-and-yaw oscillations. Hence, the flutter velocity is constant. The impact of the additional terms on T-tail flutter can be accounted for by the strip theory approach [19] and the T-tail DLM code mentioned above [20]. Both tools predict a drop in the flutter velocity with positive HTP incidence angle (up-force) by up to 16% and an increasing flutter velocity for negative HTP incidence angles (downforce). Below -1° and -2° HTP incidence angle, respectively, the T-tail DLM code and the strip theory do not yield flutter points anymore within the considered velocity range. The flutter points computed with LFD data [21] are in good agreement for positive incidence angles but show a less extreme increase in flutter velocity for negative incidence angles. An extract of these results has been published in [22].

2 Common experimental means

Besides the above described numerical methods suitable for the prediction of the integration of advanced propulsion system, the XDC demonstrator also includes the further development and demonstration of advanced experimental means for the future testing activities. Such common experimental means include the development of novel MEMS-based high frequency pressure sensors including the demonstration of their optimal integration to W/T models. This in future will enable high-resolution measurements of surface pressure fluctuations at a low price, and therefore strongly supports to prove simulation results and validate numerical tools, which are a key enabler for further design improvements. Within XDC, an improved instrumentation for vibration measurements to speed up the measurement with improved accuracy is being developed. Furthermore, the demonstration of contactless blade deformation measurements by means of IPCT in combination with optical surface pressure measurements using the pressure-sensitive paint technique is one part of XDC. These measurement techniques will enable the detailed assessment of the deformation and the surface pressure without installing sensors and cabling in the rotating system that would disturb the sensitive flow around the blades and thus distort the measurements. Finally, also optical methods to investigate the transition of the surface flow are being developed and demonstrated such as the TSP method. Examples for the latter three activities are briefly presented in what follows.

2.1 Vibration testing

Acoustic comfort for large passenger aircrafts has become a particularly important topic in the last decades. To provide design decisions that help to minimize cabin noise, it is necessary to fully understand the source generation mechanisms and the transmission paths involved.

The study of such problem presents a great challenge since any experimental analysis will require numerous flight tests for data acquisition and evaluation, which means extremely high costs for research and development. If we consider that one of the most important sources of cabin noise in the low–middle frequency range is the engine, our contribution focuses on the development of an active excitation system that will mimic the vibrational behavior of those engines. Such system will help to facilitate the vibro-acoustic research by allowing to replace flight tests by ground or laboratory tests. The developed system should be able to replicate the three-dimensional forces and moments, introduced by a real engine into an arbitrary structure, a demonstrator structure or a real wing if necessary. The system is based on a multichannel active

controller. Such system takes as input a reference model that represents the behavior of the engine and generates the control signals that are fed to the force actuators that drive the vibratory response. The moments are generated in a similar way, except for the fact that a pair of opposite forces on an attachment device is used. The control system has been developed gradually: first, a simple proof of concept was realized with a single-input single-output (SISO) force controller. Next, a multi-input multi-output (MIMO) system was able to control the injected forces in the three directions of space. Later, a multi-input single-output MISO moment control system was developed. And finally, a MIMO system that combines forces and moments control. All these incremental steps have been already described and reported in several publications [23–26]. To exemplify the work already performed, the latest force and moment MIMO implementation of the controller are shown. The test structure used was a single aluminum plate of $1 \times 0.8 \times 0.03$ m, with an asymmetric milled pattern that resembles the skin fields, stringers, and frames typically found in fuselage structures. The thickness of the skin fields, stringers and frames was 1, 5 and 10 mm respectively. The plate was suspended using bungee cords to generate free displacement boundary conditions, as seen in Fig. 13. For the evaluation of the MIMO force and moment of force control implementation, five shakers are attached, one that applies F_z and two responsible for generating the moments in M_x and M_y direction like shown in Fig. 13. In this case, three different frequency profiles were arbitrarily defined. These profiles serve as the target reference that the controller will try to replicate at the injection point of the structure. The result of the evaluation is summarized in Fig. 14, where the Reference profiles and the Control ON conditions are shown. The solid and dashed lines represent the Reference and the Control ON respectively.

There, it is possible to establish the correct operation of the controller. The good agreement among references and

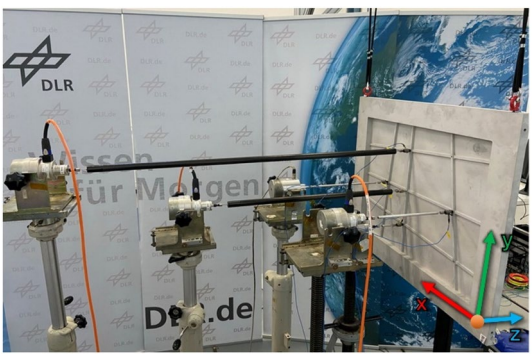

Fig. 13 Aluminum plate configuration for force and moment of force control

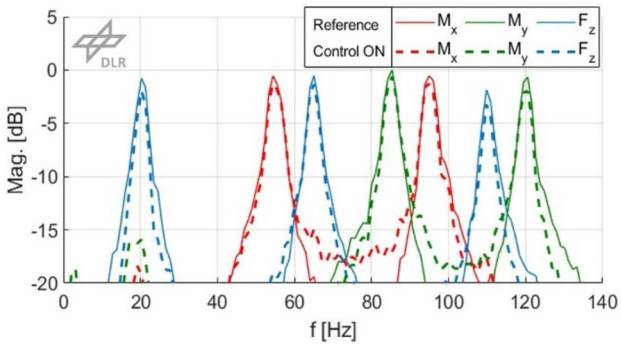

Fig. 14 Spectral comparison of Moment M_x, M_y and F_z control, Reference vs. Control ON

resulting profiles illustrates the proper generation of control force and moments. As seen there, it is also possible to notice an adequate signal-to-noise ratio of 15 dB that the system is able to generate. Future work will focus on the extension of the controller to a higher number of channel count to be able to provide all 6 degrees of freedom that fully represent a real engine.

2.2 Combined IPCT/PSP measurements

During two measurement campaigns, a surface pressure measurement applying pressure-sensitive paint (PSP) and a blade deformation measurement using the Image Pattern Correlation Technique (IPCT) [28] have been performed on a research rotor with double-swept tips [27] on the Rotor Test Rig in Göttingen (RTG). In the first campaign, a PSP coating was applied to investigate unsteady surface pressures, and in the second campaign, an IPCT pattern for contactless blade deformation measurements was applied.

The PSP measurement system comprised DLR's PSP sensor, which is capable to capture unsteady flow phenomena and an improved version of a double-shutter camera which was used in a preceding PSP rotor experiment [29], and which eliminates the problem of image blur in PSP measurements on fast rotating blades when applying the established single-shot lifetime technique [31]. The PSP coating was applied on the outer 65% of the blade suction side. Surface pressures were measured at blade-tip Mach and Reynolds numbers of $M_{tip} = 0.3$ and $Re_{tip} \sim 6 \times 10^5$ at settings with collective pitch angle only as well as at different cyclic pitch settings. The unique test setup at RTG allowed to scan the entire pitch cycle at a phase resolution of 0.225 degree azimuth. Sample results of the measured pressure footprint at three different collective pitch angles are provided in Fig. 15. In this figure, blade rotation is counter-clockwise. At $\Theta_{root} = 23$ deg, the suction peak is visible especially outboard of the blade apex at relative blade radii of $r/R > 0.77$. As the root pitch angle increases to $\Theta_{root} = 26$ deg, the blade-tip

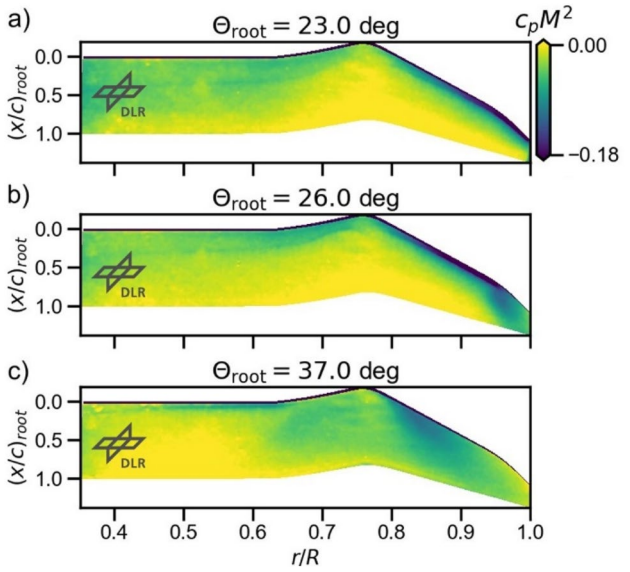

Fig. 15 Visualization of surface pressure maps using ensemble averaged PSP data evaluation at indicated collective pitch angles

vortex starts to detach from the leading edge of the backward swept outer part of the blade close to the tip, leaving a low pressure footprint at $r/R > 0.95$ (see Fig. 15b).

Further increase of the pitch angle results in flow separation both inboard and outboard of the blade apex as previously observed in numerical computations using the same rotor setup [37] and as can be observed in Fig. 15c) for the case at $\Theta_{root} = 37$ deg. For this case, a plateau-like pressure distribution evolves between $0.65 < r/R < 0.8$ next to the adjacent region further outboard at $r/R > 0.8$, where a large detached leading edge vortex still causes a gradient from lower pressures at the blade leading edge to higher pressures near the trailing edge. For the IPCT measurements, various improvements to the imaging setup and the evaluation software package achieved within the XDC were successfully demonstrated.

The imaging setup (see Fig. 16) has been extended with high-power LED-arrays operated in overdriven pulsed mode [30] to gain sufficient light intensities for the short light pulses of 3–5 µs to avoid motion blur. Furthermore, improved tools to design an optimized correlation pattern as well as a calibration procedure to determine the rotation axis of the rotor using a camera recording sequence have been applied. The stereo–image pair sequences recorded during the IPCT measurement campaign have been evaluated with the time-series evaluation implemented to the DLR-IPCT evaluation software package within XDC. To measure relative deformations, an additional post-processing tool has been enhanced to fix defined areas on the measurement area based on the 3D-displacement vector fields delivered by the time-series correlation.

The images were recorded in a phase-fixed mode as well as in scanning mode with a phase shift of 0.5° azimuth between consecutive images to test the evaluation scheme for both operation modes. Some first example results of the IPCT measurements are shown in Fig. 17. The deformation at the inner part of the evaluation area at r/R of about 0.4 were set to zero, which is marked by a blue frame in the result plots of Fig. 16. Thus, the deformations were evaluated in a blade fixed frame of reference. Although the blade is relatively stiff, the slightly larger tip displacement for the higher pitch angle is clearly visible.

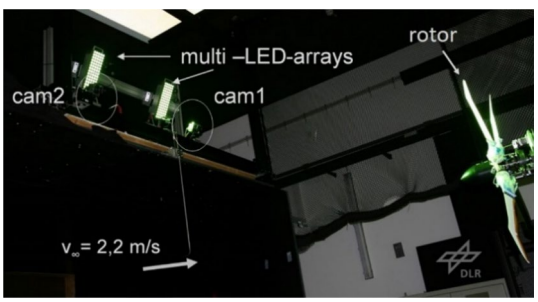

Fig. 16 IPCT measurement setup for the demonstration of blade deformation measurements

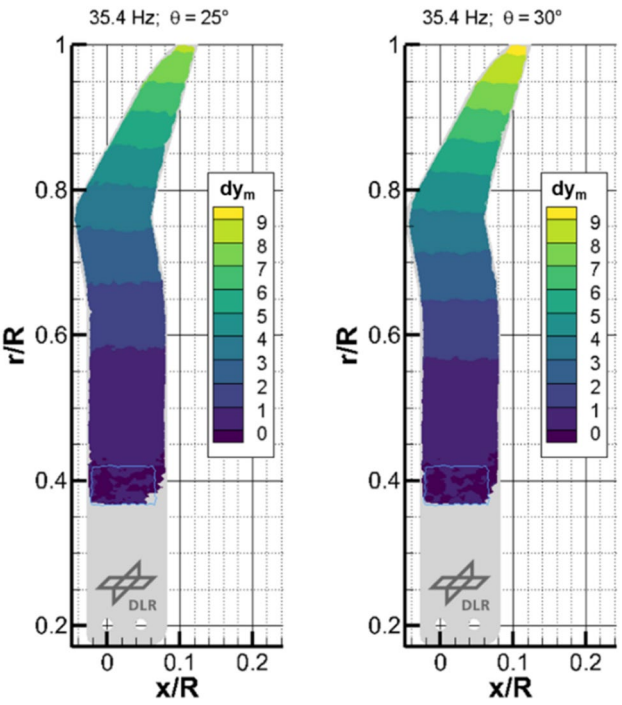

Fig. 17 IPCT Test: blade deformations dy_m in mm at a rotational speed of 35.4 Hz with different pitch settings ($\theta = 25°$ and $\theta = 30°$)

2.3 TSP measurements on the effects of steps on crossflow-dominated transition

2.3.1 SPECTRA configuration

The SPECTRA (SwePt flat PlatE Crossflow TRAnsition) configuration is a testbed for studying crossflow-dominated transition under controlled conditions. It consists of a flat plate with a Clark-Y nose profile and a displacement body arranged above it, which imprints a pressure distribution with the desired properties on the upper side of the flat plate. The pressure distribution of the flat plate is crucial for the stability properties of the boundary layer at this surface. It was designed to resemble the pressure distribution in a previously used configuration used by Bippes et al. in the 90 s and early 00 s at DLR Göttingen [31]. The boundary layer under investigation is stable toward all typical primary instabilities of a swept configuration except for crossflow instabilities [32]. This allows the research of their isolated behavior in the presence of surface imperfections such as steps. A slat arranged in front of the displacement body helps to avoid flow separation on the upper side of the displacement body. Two different displacement bodies (A and B [32]) can be used in the configuration with different corresponding pressure distributions on the flat plate.

Figure 18 shows the cross section of the SPECTRA-A configuration used in the activities, which is the topic of this article. The flat plate consists of multiple segments for different possible measurement techniques, separated in chord-wise direction (x_c). By shifting the vertical (z) position of the nose segment relative to the next segment, a forward-facing step or backward-facing step can be introduced. The location of the step is determined by the junction of the nose segment and the next segment, which is located at $x_c = 150$ mm, as indicated in Fig. 18. The total chord length of the plate is $c = 600$ mm.

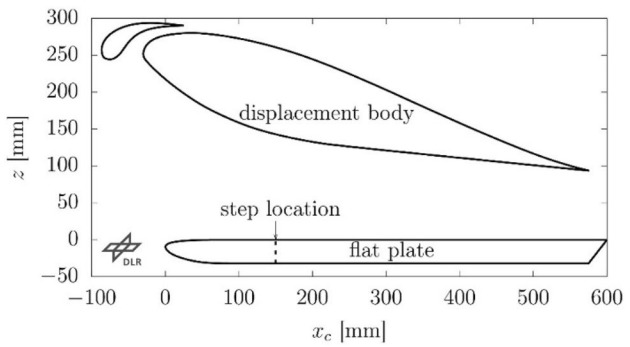

Fig. 18 Cross section of the SPECTRA-A configuration

2.3.2 Wind tunnel facility

For the investigation of the effect of steps on crossflow-dominated transition, the SPECTRA configuration is fixed with a sweep angle of 45° in the open test section of the one-meter wind tunnel at DLR Göttingen (1MG). The 1MG is a closed-circuit wind tunnel of Göttingen type with a maximum free-stream velocity of 70 m/s. In the velocity range used for this investigation, the typical turbulence level is $Tu = 0.18\%$, measured directly upstream of the SPECTRA configuration.

2.3.3 Temperature-sensitive paint

The location of the laminar-turbulent transition on the upper side of the flat plate is measured with the temperature-sensitive paint (TSP) method. The TSP method is a thermographic measurement technique, which relies on the temperature-dependent emission of luminophores [33].

When performing TSP visualizations in low-speed applications, a heat flux between the model surface and the fluid is necessary [34]. For the current experiment, an electrical model heating based on carbon nanotubes (CNT) is applied. The combination of the CNT heating and TSP is called cntTSP [35] in the following. All components of the cntTSP, i.e., the base coat, CNT, screen layer, and TSP are spray-coated into a pocket in the main segment of the flat plate. The applied cntTSP provides the possibility to perform flow visualizations between $0.26 \leq x/c \leq 0.90$, i.e., a length of 0.38 m, and a span-wise extent of 0.8 m. The TSP acquisition system, i.e., the LEDs to illuminate the luminophores and cameras to record the emitted phosphorescence light, is integrated into the displacement body. Since, the internal volume of the displacement body does not provide sufficient space for scientific cameras and standard LEDs for TSP measurement, a miniaturization of the LEDs and cameras was necessary [36]. This is achieved by applying machine vision cameras and installing only the LED chip inside of the displacement body. To acquire the entire cntTSP-coated area, four cameras together with a single-board computer for each camera are installed in the displacement body. Also, five LEDs with suitable emission characteristics are integrated.

2.3.4 Exemplary results

The influence of backward-facing steps on the crossflow instability is derived from the TSP visualization results. Two examples of TSP visualization results are shown in Figs. 19 and 20. Brighter color corresponds to laminar regions, whereas darker color indicates larger skin friction than the laminar boundary layer. An increased skin friction is caused by turbulent flow or by crossflow vortices. The crossflow

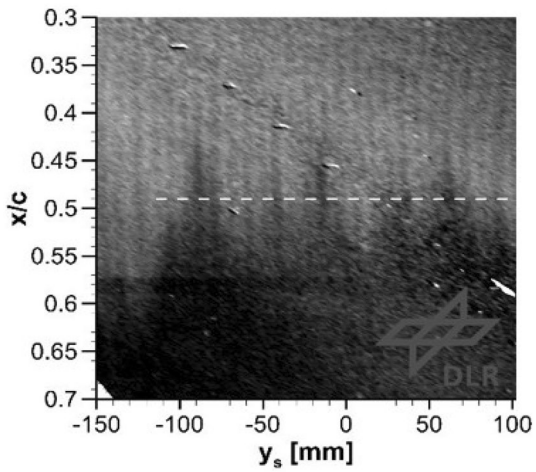

Fig. 19 TSP result without a step at a set wind tunnel velocity of 31.0 m/s

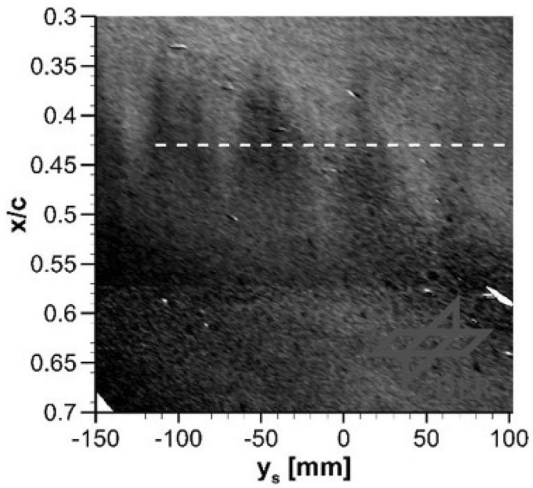

Fig. 20 TSP result of a backward-facing step of 0.45 mm height at a set wind tunnel velocity of 31.0 m/s

vortices are excited by a span-wise row of periodically arranged discrete roughness elements close to the leading edge with a span-wise spacing of $\lambda = 10$ mm. The stationary crossflow vortices generate the long straight lines, which are visible in Fig. 20. A comparison of Figs. 19 and 20 represents the effect of a backward-facing step of $h = 0.45$ mm on the footprint of the stationary crossflow vortices and the transition front at a fixed free-stream velocity. The transition front moves upstream from a spanwise average location of $x_{tr,ref}/c = 0.49$ to $x_{tr,step}/c = 0.43$, while the spanwise variation of the local transition location increases.

3 Conclusions and summary

On the previous pages, a brief overview about the development work performed within the XDC demonstrator of the CleanSky 2 LPA Platform 1 is given. As far as this demonstrator is twofold, the presented examples have been divided into a common numerical and a common experimental part. With respect to the numerical part, aero-acoustic investigations on the noise emission of an installed UHBR as well as the prediction of the jet-flap interference noise have been briefly described. Moreover, the impact of rotational terms appearing in a rotating reference frame (i.e., centrifugal and Coriolis accelerations) on the transition mechanisms for the Z49 rotor blade has been investigated by means of linear stability computations. It is found that rotation hardly affects the instability characteristics of Tollmien–Schlichting waves. On the other hand, rotation destabilizes the cross-flow instabilities, but not enough to trigger cross-flow-dominated transition in the investigated operating condition. As a third example, the fan design work aided by numerical tools was presented. Last but not least, simulations related to the creation of an aeroelastic model of a reference configuration and a flutter analysis were described.

With regard to the experimental stream of the XDC and related to the field of vibro-acoustics, the development of an active excitation system replicating the vibrational behavior of engines is shown. This system will help reduce the amount of flight tests and will accelerate vibro-acoustic cabin noise research. Such system will provide an important tool for vibro-acoustic cabin noise research in future and will help better understand advanced propulsion concepts and their interaction and integration with the airframe. With respect to non-intrusive measurements, the determination of unsteady surface pressure using iPSP and deformation using IPCT has been demonstrated on a research rotor with double-swept tips. The rotor blades only had to be painted with the pressure-sensitive paint and the IPCT pattern, but no flow disturbing and time-consuming sensor installation had to be done. Thus, it is proposed to perform pressure and deformation measurements on rotors in future in a similar manner to minimize the installation effort and the flow disturbance. Finally, exemplary results of TSP measurements for the investigation of effects of steps on crossflow-dominated transition have been described.

Summing up, the XDC demonstrator is a valuable collection with regard to the recent developments of numerical and experimental tools for the simulation and measurement challenges of the future propulsion systems and aircraft configurations.

Acknowledgements The authors would like to thank all helping hands that enable the performance of the work presented in this paper. This project has received funding from the Clean Sky 2 Joint Undertaking

(JU) under grant agreement No. 945583. The JU receives support from the European Union's Horizon 2020 research and innovation program and the Clean Sky 2 JU members other than the Union. The provision of the laminar basic flow in Sec. 2.1.1 by Airbus is gratefully acknowledged. Part of this work has been presented previously in [15].

Funding Open Access funding enabled and organized by Projekt DEAL.

Data availability statement In order to provide these developments to the community a final workshop will take place in autumn 2023 and the proceedings will be published through a book.

References

1. Delfs, J. W., Bauer, M., Ewert, R., Grogger, H. A., Lummer, M., & Lauke, T. G.: Numerical Simulation of Aerodynamic Noise with DLR's aeroacoustic code PIANO, PIANO, Vol. Handbook version 5.2 (2008)
2. Stuermer, J.Y.: The Case for Counter-Rotation of Installed Contra-Rotating Open Rotor Propulsion Systems, AIAA 2012–2785, 30th Applied Aerodynamics Conference. Lousiana, USA, New Orleans (2012)
3. Dierke, J., Akkermans, R., Delfs, J., Ewert, R.: Installation effects of a propeller mounted on a wing with coanda flap. Part II: Numerical investigation and experimental validation, AIAA 2014–3189, 20th AIAA/CEAS Aeroacoustics Conference, Atlanta, Georgia, USA (2014)
4. Cheng, Z., Yan, Y., Tao, Z., Haibo, D., Guoxiang, H.: A sharp interface immersed boundary method for flow-induced noise prediction using acoustic perturbation equations, Computers & Fluids, Reference: CAF 105032 (2021)
5. Ewert, R., Dierke, J., Neifeld, A.: Simulation of Cold Jet Installation Noise using a Stochastic Backscatter Model, AIAA 2017–3017, 23rd AIAA/CEAS Aero-acoustics Conference, Denver, Colorado, USA (2017)
6. Neifeld, R., Ewert: Jet-Wing interaction noise prediction with forced Eddy simulation, WAVES 2019, Wien, Österreich (2019)
7. Dechamps, X., Hein, S.: Extension of the PSE Code NOLOT for Transition Analysis in Rotating Reference Frames. New Results in Numerical and Experimental Fluid Mechanics XI: Contributions to the 20th STAB/DGLR Symposium. Springer, Brunswick, Germany, pp. 179–188 (2017)
8. Kruse, M., Munoz, F., Radespiel R.: Transition prediction results for sickle wing and NLF(1)-0416 test cases. 2018 AIAA Aerospace Sciences Meeting, AIAA Paper 2018-0537 (2018)
9. https://cleansky.virtualfair.be/hangar
10. Schnell, R., Goldhahn, E., Julian, M.: Design and performance of a low fan-pressure-ratio propulsion system. ISABE conference 2019–24017, **16** (2019)
11. Schnell, R., Frey, C.: Acoustic impact on fan flutter in short aero engine intakes, AIAA aviation forum (2021)
12. Krüger, W. R., Ciampa, P. D., Geier, M., Kier, T., Thiemo, T., Klimmek, T., Kohlgrüber, D., Ohme, P., Risse, K., Schwinn, J.: A comprehensive loads process at the DLR - definition, analysis, experimental evaluation. Aerospace Lab, 14. Onera Scientific Information Department. https://aerospacelab.onera.fr/al14/comprehensive-load-process-at-the-dlr-definition-analysis-and-experimental-evaluation (2018)
13. Klimmek, T., Schulze, M., Abu-Zurayk, M., Ilic, C., Merle, A.: cpacs-MONA – An independent and in high fidelity based MDO tasks integrated process for the structural and aeroelastic design for aircraft configurations. IFASD 2019 - International Forum on Aeroelasticity and Structural Dynamics, 10th – 13th of June 2019, Savannah, GA (USA) (2019)
14. Klimmek, T.: Parametric set-up of a structural model for FERMAT configuration for aeroelastic and loads analysis. Journal of Aeroelasticity and Structural Dynamics, **3**(2), Seiten 31–49. Department of Aerospace Engineering of Politecnico di Milano (2014)
15. Krüger, W. R., Boden, F., Kirmse, T., Lemarechal, J., Schröder, A., Barth, H. P., Oertwig, S., Siller, H., Delfs, J. W., Moreau, A., Schäfer, D., Stürmer, A., Norambuena, M. A.: Common numerical methods & common experimental means for the demonstrators of the large passenger aircraft platforms. AEC2020 - Aerospace Europe Conference, 25–28. Bordeaux, France (2020)
16. Norambuena, M. A., Böswald, M., Govers, Y.: Vibro-acoustic analysis of flight test data comprising fuselage vibrations, external pressure and interior cabin noise measurements. 54th AIAA Aerospace Sciences Meeting (2016)
17. Jennings, W. P., Berry, M. A.: Effect of Stabilizer dihedral and static lift on T-tail flutter. Journal of Aircraft, Bd. 14, pp. 364–367, 4 (1977)
18. Murua, J., Zyl, L., Palacios, R.: T-Tail flutter: Potential-flow modelling, experimental validation and flight tests. Progress in Aerospace Sciences, Bd. **71**, pp. 54–84, (2014)
19. Queijo M. J.: Theory for computing span loads and stability derivatives due to sideslip, Yawing, and rolling for wings in subsonic compressible flow (1968)
20. Zyl, L., Mathews, E. H.: Aeroelastic analysis of T-tails using an enhanced doublet lattice method. Journal of Aircraft, Bd. 48, pp. 823–831, 5 (2011)
21. Thormann, R., Widhalm, M.: Linear-frequency-domain predictions of dynamic-response data for viscous transonic flows. AIAA Journal, Bd. 51, pp. 2540–2557 (2013)
22. Schäfer und, D., Arnold, J.: Assessment of T-tail flutter using an enhanced potential flow theory approach and linearized frequency domain CFD data. IFASD 2019 - International Forum on Aeroelasticity and Structural Dynamics (2019)
23. Norambuena, M., Winter, R.: Active structural excitation as known source for structure-borne noise research. INTER-NOISE 2019. Madrid: International Institute of Noise Control Engineering (I-INCE) (2019)
24. Norambuena, M., Winter, R.: An adaptive structural excitation system as a tool for structure-borne noise research. ICA 2019 - 23rd International Congress on Acoustics. Aachen: Deutsche Gesellschaft für Akustik e.V. (DEGA) (2019)
25. Norambuena, M., Winter, R.: Biedermann, J. Accurate structural excitation through adaptive control. International Conference on Noise and Vibration Engineering ISMA 2018. Leuven (2018)
26. Norambuena, M., Winter, R.: Biedermann, J.: Inverse control applied to structural excitation systems. DAGA 2018 - 44. Jahrestagung für Akustik. München (2018)
27. Müller, M.M., Schwermer, T., Mai, H., Stieg, C.: Development of an innovative double-swept rotor blade-tip for the rotor test facility

¨ Goettingen", DLRK 2018 - Deutscher Luft- und Raumfahrtkongress, 4^{th} – 6^{th} of September 2018. Friedrichshafen, Germany (2018)
28. Boden, F., Kirmse, T., Jentink, H.: Image pattern correlation technique (IPCT). In: AIM2 Advanced Flight Testing Workshop - HANDBOOK of ADVANCED IN-FLIGHT MEASUREMENT TECHNIQUES BoD – Books on Demand, Norderstedt, Germany. ISBN 978-3-7322-3740-1 (2013)
29. Weiss, R., Geisler, T., Schwermer, D., Yorita, U., Henne, C., Klein, M.R.: Single-shot pressure-sensitive paint lifetime measurements on fast rotating blades using an optimized double-shutter technique. Exp. Fluids **58**, 120–140 (2017)
30. Stasicki, B., Schröder, A., Boden, F., Ludwikowski, K.: High-power LED light sources for optical measurement systems operated at continuous and overdriven pulsed mode. EOM17 SPIE Optical Metrology, 25th – 29th of June 2017, Munich, Germany (2017)
31. Bippes, H.: Basic experiments on transition in three-dimensional boundary layers dominated by crossflow instability. Prog. Aerosp. Sci. **35**, 363–412 (1999)
32. Barth, H. P., Hein, S., Rosemann, H.: redesigned swept flat-plate experiment for crossflow-induced transition studies. Notes on numerical fluid mechanics and multidisciplinary design; Springer International Publishing, pp. 155–165 (2017)
33. Liu, T., Sullivan, J.P., Asai, K., Klein, C., Egami, Y.: Pressure and temperature sensitive paints. Springer-Verlag (2021)
34. Fey, U., Egami Y.: Transition-detection by temperature-sensitive paint. Springer Handbook of Experimental Fluid Mechanics, Springer-Verlag, Berlin, Heidelberg, New York, pp. 537–552 (2007)
35. Klein, C., Henne, U., Sachs, W., Beifuß, U., Ondrus, V., Bruse, M., Lesjak, R., Löhr, M.: Application of carbon nanotubes (CNT) and temperature-sensitive paint (TSP) for the detection of boundary layer transition. AIAA2014–1482 52nd Aerospace Sciences Meeting, 13–17 January 2014, National Harbor, USA (2014)
36. Grebory, J. W., Kumar, P., Peng, D., Fonov, S., Crafton, J., Liu, T.: Integrated optical measurement techniques for investigation of fluid-structure interactions. 39th AIAA Fluid Dynamics Conference, San Antonio, Texas, June 22–25 (2009)
37. Kaufmann, K., Müller, M.M., Gardner, A.D.: Dynamic stall computations of double-swept rotor blades. New results in numerical and experimental fluid mechanics XII: Contributions to the 21th STAB/DGLR Symposium. Springer, Darmstadt, Germany **142**, 351–361 (2020)